THE JOURNAL OF PHYSICAL CHEMISTRY A

Article

pubs.acs.org/JPCA

Influence of Combustion Conditions on Hydrophilic Properties and Microstructure of Flame Soot

Chong Han, Yongchun Liu,* Chang Liu, Jinzhu Ma, and Hong He*

Research Center for Eco-Environmental Sciences, Chinese Academy of Sciences, Beijing, 100085, China

ABSTRACT: Previous studies suggest that structure and reactivity of soot depend on combustion conditions like the fuel/oxygen ratio and nature of fuels. However, the essence of how combustion conditions affect physical and chemical properties of soot is still an open question. In this study, soot samples were prepared by combusting toluene, *n*-hexane, and decane under controlled conditions, and their hydrophilic properties, morphology, microstructure, content of volatile organic compounds, and functional groups were characterized. The hydrophilicity of *n*-hexane and decane flame soot increased with decreasing fuel/oxygen ratio, while it almost did not change for toluene flame soot. Fuel/oxygen ratio had little effect on the morphology of aggregates and the graphite crystallite size. The primary particle size and the content of volatile organic compounds on soot decreased with decreasing fuel/oxygen ratio. Less hydrophobic groups (C−H) and more hydrophilic groups (C═O) were observed on lean *n*-hexane and decane flame soot than that on the corresponding rich flame soot. Volatile organic compounds had little effect on the hydrophilicity of soot while the hydrophilicity correlated linearly with the ratio of C═O content to C−H content. The hydrophilic functional groups were found to be mainly located at graphene layer edges and on surface graphene layers in soot.

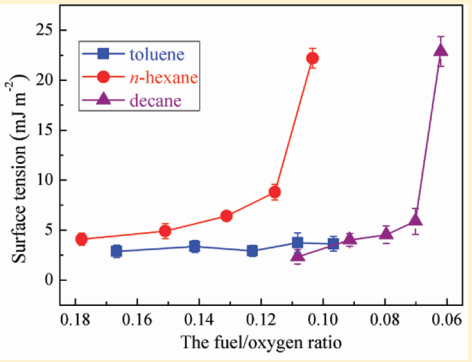

1. INTRODUCTION

Soot aerosols have an important influence on the atmospheric radiative balance by directly absorbing solar radiation as well as by indirectly scattering solar radiation as cloud condensation nuclei (CCN).[1,2] It has been reported that soot may be responsible for the increase of droughts in the northeast and floods in the southeast in China in the summer over the past 20 years.[2] The contribution of soot to global warming may be second only to that of CO_2.[3] Soot also poses a health risk by causing and enhancing respiratory, cardiovascular, and allergic diseases.[4] In addition, soot particles are expected to be active in heterogeneous reactions with gaseous pollutants like NO_2, H_2SO_4, and O_3[5−9] significantly affecting the chemical composition of the atmosphere and thus influencing their climatic and health effects. Many previous studies imply that the environmental effects and the reactivity of soot are greatly influenced by combustion conditions, such as fuel/oxygen ratio and nature of fuels.[10−14]

In previous research, the morphology, microstructure, and chemical composition of soot particles, including flame soot,[15,16] spark discharge soot,[17,18] and commercially available soot,[17−19] have been investigated using combinations of several methods. It has been shown that soot is composed of chainlike agglomerates of primary particles,[17] which consist of perturbed graphitic layers oriented concentrically in an onionlike fashion.[18] Functional groups, including aliphatic or aromatic C−H, carbonyl C═O, and ethers C−O, have been confirmed through infrared spectroscopy.[13,20,21] Microstructures including graphitic carbon, disordered carbon, and amorphous carbon have also been detected using Raman spectroscopy.[15−17,19,22,23] Recent studies have shown that residence time in the flame and flame temperature can induce modifications in the microstructures and functional groups of soot.[15,20] Thus, this demonstrates that the structure and properties of soots should greatly depend on their formation conditions. On the other hand, the CCN and ice nuclei (IN) abilities of soot particles significantly depend on their hydrophilicity. Although several previous studies have investigated the water uptake behavior of soot particles,[16,23−25] little attention has been paid to the quantitative relationships among hydrophilicity, structure, and composition of soot produced under different combustion conditions.

In this study, toluene, *n*-hexane, and decane soot samples were produced under well-controlled combustion conditions. Hydrophilic changes due to different combustion conditions were studied by analyzing surface tension derived from contact angle. The morphology and microstructure of soot were investigated using transmission electron microscopy (TEM) and Raman spectroscopy. Surface-bonded volatile organic compounds (VOCs) and functional groups were also studied by thermogravimetric (TG) analysis and single reflection attenuated total internal reflection infrared (ATR-IR) spectra. Finally, the quantitative relationship relating the hydrophilic properties, structure, and chemical composition of soot was discussed.

Received: February 1, 2012
Revised: March 29, 2012
Published: March 29, 2012

2. EXPERIMENTAL SECTION

2.1. Soot Production. Soot samples were produced by burning toluene, *n*-hexane, and decane (AR, Sinopharm Chemical Reagent Lo., Ltd.) in a coflow homemade burner system as described by Rossi and co-workers.[10,26,27] The coflow burner consisted of a diffusion flame maintained in a flow of synthetic air, which was controlled by mass flow meters to regulate the fuel/oxygen ratio. The airflow consisted of high pure oxygen and nitrogen and the oxygen/nitrogen ratio was in the range of 27.5−47.5%. The fuel was fed by a cotton wick extending into the liquid fuel reservoir. The fuel/oxygen ratio, which was the molar ratio of fuel (measured by consumed fuel mass) to oxygen (obtained by the entrained air flow volume), was in the range of (0.170−0.095), (0.180−0.100), and (0.110−0.060) for toluene, *n*-hexane, and decane. Thus, soot obtained in a relatively high fuel/oxygen ratio (0.170 for toluene, 0.180 for *n*-hexane, 0.110 for decane) was roughly identified as rich flame soot, while one produced in a relatively low fuel/oxygen ratio (0.095 for toluene, 0.100 for *n*-hexane, 0.060 for decane) was roughly identified as lean flame soot. Soot was collected on aluminum foil suspended over the diffusion flame.

2.2. Characterization of Soot. The hydrophilicity of soot was investigated by measuring contact angle, which was defined geometrically as the angle formed at the liquid, gas, and solid phase boundary. Before the contact angle measurements, 10 mg of the fresh fluffy soot powder was pressed into a sheet of 13 mm diameter at a slight compacting pressure. Then, a water droplet with radius around 2 mm was immediately dropped on the soot sheet. The contact angle of the water droplet on the soot sheet was determined using sessile drop measurement, which has been extensively used.[24,28−31] After the water was dropped on the soot sheet, a picture of the spreading water on the soot sheet was taken using a Sony digital camera.[24]Then, the contact angle of the water droplet was measured with ImageJ 1.41 software.

The morphology and particle size of the soot were examined using a TEM (H-7500, Hitachi). Soot produced in a diffusion flame was directly deposited onto a Cu microgrid. The acceleration voltage was set to 200 kV for the measurements. ImageJ 1.41 software was used to analyze the diameter of soot particles.

Raman spectra of soot were recorded on a UV resonance Raman spectrometer (UVR DLPC-DL-03), which was described previously.[23] A continuous diode-pumped solid state (DPSS) laser beam (532 nm) was used as the exciting radiation with a source power of 40 mW. No sample modification was observed when the sample was irradiated under the experimental conditions. The diameter of the laser spot on the sample surface was focused at 25 μm. The spectra resolution was 2.0 cm^{-1}. The exposure time for each scan was 50 s.

The content of VOCs on these three flame soots was investigated by thermal desorption using a commercial TG instrument (TGA/DSC1/HT1600, Mettler-Toledo Co., Ltd.). The amount of VOCs lost from the soot was recorded when the temperature was ramped from 30 to 300 at 10 °C min^{-1} in nitrogen flow.

The functional groups of the samples were characterized using a Fourier transform infrared spectrometer (FT-IR, NEXUS 6700, Thermo Nicolet Instrument Corp.) equipped with a high-sensitivity mercury−cadmium−telluride (MCT) detector cooled by liquid N_2 and an ATR-IR cell. The spectra of soot were recorded (32 scans, 4 cm^{-1} resolution) using the blank Ge crystal as reference.

3. RESULTS

3.1. Hydrophilicity of Soot. The value of contact angle, which can be used as an indicator of the hydrophilicity of materials, depends on the strength of the interaction between water droplets and the material surfaces. A water droplet giving a small contact angle implies a hydrophilic solid surface, while hydrophobic surfaces yield large contact angles. Figure 1 shows

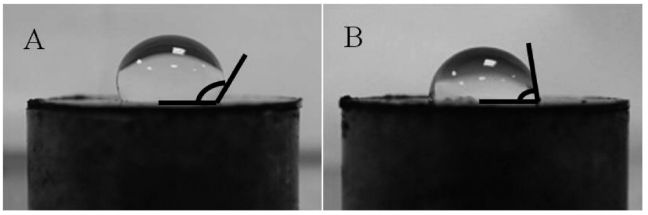

Figure 1. Pictures of water droplets deposited on rich (A) and lean (B) *n*-hexane flame soot.

the pictures of water droplets on the surfaces of the rich and lean *n*-hexane flame soot. The water droplet on the lean flame soot displayed a less spherical shape than that on the rich flame soot suggesting an increase in hydrophilicity of *n*-hexane flame soot with decreasing fuel/oxygen ratio. Through comparing previous reports,[24,32] it was found that the contact angles of lean *n*-hexane and decane soot were similar to ones of propane and kerosene soot indicating that they have similar hydrophilicity.

The changes of contact angle indicate that the surface free energies between water and soot are altered with the decreasing fuel/oxygen ratio. Surface free energies are extremely important since they not only determine the strength of interaction between water and solid surfaces but also control the dynamics of molecular self-assembly, wetting, spreading, and adhesion.[31] Therefore, surface free energies are taken as a key factor to understanding the mechanism of surface-based phenomena. The solid surface tension γ_{sv}, which is proportional to surface free energy, can be determined using Young's equation.[31]

$$\gamma_{lv} \cos\theta = \gamma_{sv} - \gamma_{sl} \quad (1)$$

where θ is the contact angle, and γ_{lv}, γ_{sv}, and γ_{sl} are the interfacial tensions of the liquid−vapor, solid−vapor, and solid−liquid interfaces, respectively. However, only γ_{lv} and θ can be experimentally measured. Thus, to determine the solid surface tension γ_{sv}, Kwok and Neumann have obtained one known equation applying the Berhelot geometrical rules[33]

$$\gamma_{sv} = \frac{\gamma_{lv}(\cos\theta + 1)^2}{4} \quad (2)$$

where γ_{lv} is the surface tension of water at ambient temperature (72.7 mJ m^{-2}).[33]

The surface tensions for these three fuels' flame soot were calculated using eq 2 and are summarized in Figure 2. A larger surface tension means that particles are more hydrophilic. It can be seen that, for *n*-hexane and decane flame soot, solid surface tensions exhibited a significant increase with decreasing fuel/oxygen ratio, while little change was observed for toluene flame soot. These results highlight differences in the roles of

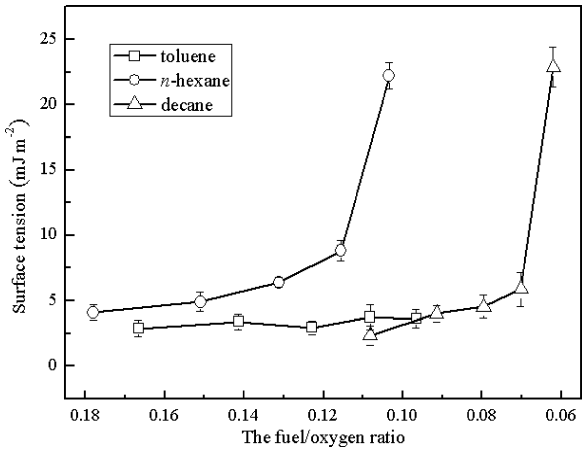

Figure 2. Plot of solid surface tension versus fuel/oxygen ratio.

combustion conditions in determining hydrophilicity for soot of different origins. The different hydrophilicity as well as the response to the fuel/oxygen ratio for these three fuels' soot implies a different content of hydrophilic or polar species formed on these soot samples. Several studies measured hydrophilicity of soot using water vapor adsorption isotherms.[16,23−25] To compare surface tension in this work with soot hydrophilicity obtained using water vapor adsorption isotherms, the following equation can be derived from the adsorption heat measured using adsorption isotherms, Young's equation, and the definition of Gibbs free energy.

$$-\gamma_{lv}(1 + \cos\theta) = Q_1 - T\Delta S \quad (3)$$

where Q_1 is adsorption heat that can be obtained through Brunauer−Emmett−Teller (BET) equation fitting, T is temperature, and ΔS is entropy change. Here, the relationship between the contact angle and the adsorption heat can be established in theory. If the part $T\Delta S$ in eq 3 is similar in the similar systems, a small contact angle (θ) should correspond to a large Q_1. Thus, we can qualitatively compare surface tension in this work with soot hydrophilicity obtained using water vapor adsorption isotherms. Unfortunately, the ΔS is unavailable at present date, and so we cannot quantitatively compare them.

It has been reported that structures and compositions can significantly affect the physical and chemical properties of soot. To identify the causes that may induce the changes in soot hydrophilicity, TEM, Raman spectra, TG, and ATR-IR spectra were used to obtain comprehensive information on the morphology, microstructure, VOCs content, and functional groups of soot produced under different combustion conditions.

3.2. Morphology and Microstructure. *Morphology of Soot Agglomerates.* Figure 3 shows TEM images of fresh rich and lean flame soot samples. All soot samples consisted of typical spherical particles, which formed long chainlike agglomerates as reported in other studies.[13,17,18] To evaluate the aggregation properties of soot samples, the ratio of maximum length (L) to average width of aggregates (W), the average particle diameter ($\bar{d}_p$), and the fractal dimension (D_f) were calculated. For fractal-like aggregates, the parameter D_f has been widely used to describe particle morphology.[23] In addition, coagulation dynamics and optical properties of soot have often been assessed using the parameter D_f, which is calculated by the following empirical and statistical relationships[23]

$$N \cong (d_a/\bar{d}_p)^{2a} \cong (L/\bar{d}_p)^{D_f} \quad (4)$$

where N is the number of primary particles in an aggregated sample, $d_a = (4A_a/\pi)^{1/2}$ is the area-equivalent diameter of the aggregated area (A_a), $a = 1.09$ is a parameter to account for the particle screening on projected TEM images, and L is the measured maximum aggregate length.

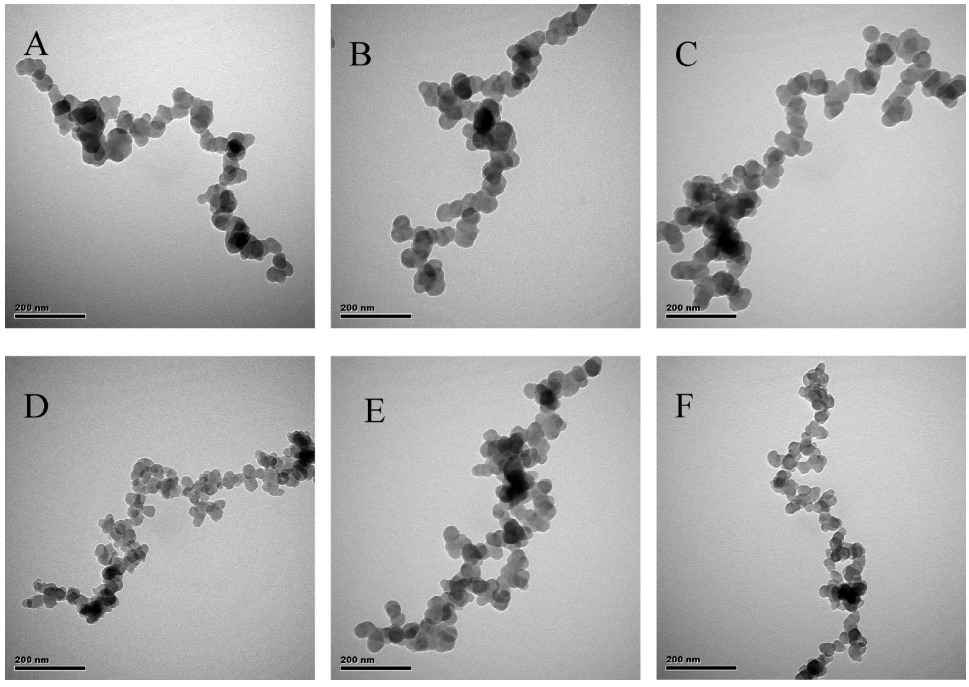

Figure 3. A, B, and C are TEM images of rich soot for toluene, *n*-hexane, and decane, respectively; D, E, and F are TEM images of lean soot for toluene, *n*-hexane, and decane, respectively.

dx.doi.org/10.1021/jp301041w | J. Phys. Chem. A 2012, 116, 4129−4136

As shown in Table 1, for all rich and lean flame soot from toluene, *n*-hexane, and decane, the parameters L/W and D_f were around 7.0 and 1.4, respectively. The values of the parameter L/W were significantly greater than that of Degussa Printex U (2.0−3.0)[23] exhibiting a longer chainlike agglomerated structure. Although the D_f parameters of soot in this work were slightly smaller than that (1.7) of ethylene and propane flame soot,[34,35] all of these studies found that D_f is insensitive to combustion conditions. A larger D_f means that the sample is prone to coagulation and reconstruction. D_f remained almost unchanged with decreasing fuel/oxygen ratio suggesting that the fuel/oxygen ratio has little effect on the formation of compacted aggregates and the growth of secondary particles. Compared to the average particle diameter ($\bar{d}_p$) of fresh rich toluene, *n*-hexane, and decane flame soot, however, the average particle diameter of all three lean flame soots showed an obvious decrease. This result coincides well with results reported by Slowik.[34] The decrease amplitude in $\bar{d}_p$ was 17.3%, 10.3%, and 16.5%. Figure 4 shows the diameter distribution of primary particles from the three fuels. The proportion of spherical particles with small diameter (<30 nm) for lean flame soot was significantly greater than that for rich flame soot, while the opposite was observed for large particles (>30 nm).

Table 1. Ratio of Maximum Length (L) to Average Width of Aggregates (W) and Average Particle Size ($\bar{d}_p$) and the Fractal Dimension (D_f) of Fresh Toluene, *n*-Hexane, and Decane Soot

fuels	type of soot	L/W	$\bar{d}_p$ (nm)	D_f
toluene	rich	5.8 ± 1.1	30.1 ± 8.7	1.42 ± 0.12
	lean	7.5 ± 0.9	24.9 ± 8.1	1.32 ± 0.10
n-hexane	rich	6.0 ± 1.2	33.1 ± 8.1	1.47 ± 0.03
	lean	7.1 ± 1.9	29.7 ± 7.0	1.44 ± 0.07
decane	rich	7.6 ± 1.3	28.4 ± 9.6	1.45 ± 0.05
	lean	7.3 ± 0.9	23.7 ± 5.9	1.37 ± 0.06

Microstructure of Soot. Figure 5 shows the first-order Raman spectra of three rich flame soots, which display well-known bands of soot near 1580 (*G* band) and 1360 cm^{-1} (*D* band). The *G* band is a typical characteristic of crystalline graphite, while the *D* band is only observed for disordered graphite. A detailed analysis of the first-order Raman spectra was performed using the five-band fitting procedure proposed by Sadezky.[19] Four Lorentzian-shaped bands (*D1*, *D2*, *D4*, and *G*, centered at about 1360, 1620, 1180, and 1580 cm^{-1}, respectively) and one Gaussian-shaped band (*D3*, centered at around 1500 cm^{-1}) were used in the curve-fitting process.[19,22,23] The *D1* band arises from the A_{1g} symmetry mode of the disordered graphitic lattice located at the graphene layer edges. The *D2* band is attributed to the E_{2g} symmetry stretching mode of the disordered graphitic lattice located at surface graphene layers. The *D3* band originates from the amorphous carbon fraction of soot. The *D4* band is related to the A_{1g} symmetry mode of the disordered graphitic lattice or C−C and C═C stretching vibrations of polyene-like structures. The *G* band is assigned to the ideal graphitic lattice with E_{2g} symmetry vibration mode.

As shown in Figure 5, the curve-fitting results (red line) for the three rich flame soots coincide well with the experimental

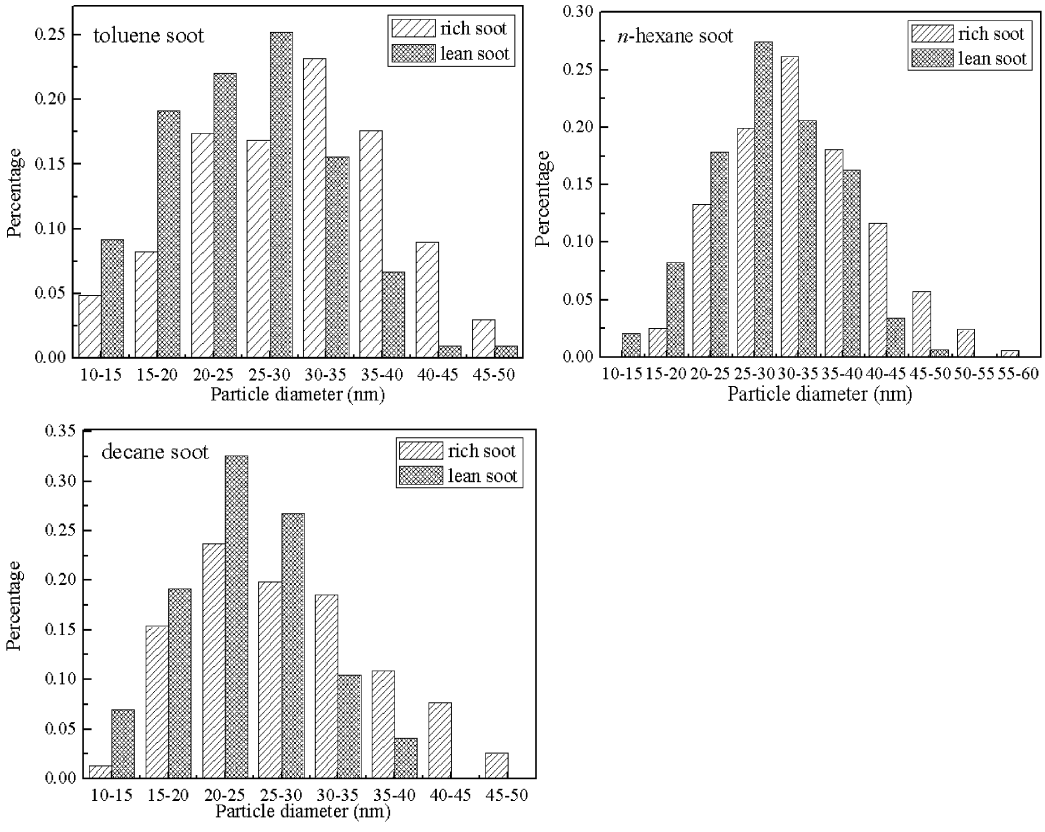

Figure 4. Diameter distribution of fresh rich and lean toluene, *n*-hexane, and decane soot.

dx.doi.org/10.1021/jp301041w | J. Phys. Chem. A 2012, 116, 4129−4136

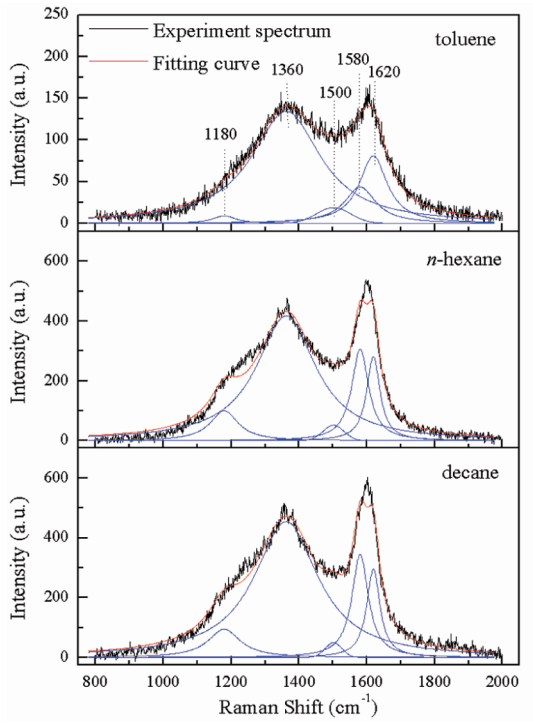

Figure 5. Raman spectra of rich toluene, *n*-hexane, and decane flame soot.

curve (black line). The correlation coefficients are greater than 0.980. We focused predominantly on discussion of changes in three bands (*D1*, *D2*, and *G*). Table 2 summarizes the intensity

Table 2. Parameters I_{D1}/I_G, I_{D2}/I_G, and L_a of Rich and Lean Toluene, *n*-Hexane, and Decane Flame Soot

fuels	type of soot	I_{D1}/I_G	I_{D2}/I_G	L_a (Å)
toluene	rich	6.2 ± 0.1	1.7 ± 0.1	17.4 ± 0.5
	lean	8.0 ± 0.2	2.2 ± 0.1	17.5 ± 1.0
n-hexane	rich	4.5 ± 0.3	0.8 ± 0.1	14.2 ± 0.3
	lean	5.5 ± 0.1	1.1 ± 0.1	14.0 ± 0.2
decane	rich	4.6 ± 0.1	0.7 ± 0.1	15.5 ± 0.3
	lean	7.2 ± 0.3	2.0 ± 0.1	16.2 ± 0.4

ratios I_{D1}/I_G and I_{D2}/I_G for different types of soot samples. Compared to the value of I_{D1}/I_G and I_{D2}/I_G for rich toluene, *n*-hexane, and decane flame soot, the values for the three lean flame soots exhibited increases. This suggests that the content of disordered carbon at graphene layer edges and surface graphene layers increases with decreasing fuel/oxygen ratio. It also implies that the lean flame soot has a lower degree of order than rich flame soot, which can be ascribed to higher degree of soot oxidation in lower fuel/oxygen ratio.[36]

For the integral intensity ratio (I_D/I_G) of *D* and *G* bands and the graphite crystallite size L_a, an empirical correlation has been derived. It was found that the ratio I_D/I_G is inversely proportional to the graphite crystallite size L_a[37,38]

$$\frac{44}{L_a} = \left(\frac{I_D}{I_G}\right) \quad (5)$$

where L_a is the graphite crystallite size as determined by X-ray. The intensities of *D* and *G* bands have been widely determined using the sum of *D1* and *D4* bands and the sum of *D2* and *G* bands.[17] By using eq 5, L_a was calculated and was found to vary between 14 and 18 Å within the standard deviation, which was consistent with the upper limit (15−20 Å) reported by Shroder and Nemanich.[39] However, L_a is smaller than the sizes of the graphite crystallite size in diesel and candle soot.[36] For all rich and lean soots, L_a essentially did not change with the fuel/oxygen ratio. This indicates that the fuel/oxygen ratio has little effect on graphite crystallite size.

3.3. Chemical Composition. *VOCs Content of Different Soot.* Heating soot samples to 300 °C should cause loss of VOCs without the bulk elemental carbon being modified.[13] Figure 6 shows a decreasing trend for the content of VOCs on

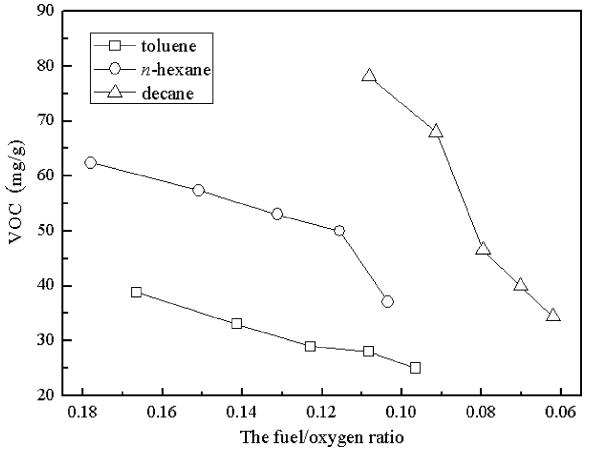

Figure 6. Changes of VOCs on fresh toluene, *n*-hexane, and decane soot with fuel/oxygen ratio.

these three fuels' soot with decreasing fuel/oxygen ratio, which is also found in previous studies.[34,35] This confirms that less VOCs are bonded on soot produced under combustion conditions with low fuel/oxygen ratio. This can be well understood since a low fuel/oxygen ratio should have high combustion efficiency for fuels thus leading to less VOCs on soot. However, the decrease in amplitude of the content of VOCs for toluene soot was significantly less than that for *n*-hexane and decane soot. Therefore, it can be concluded that toluene soot has less associated volatile organic carbon than *n*-hexane and decane soot.

Functional Groups. Figure 7 shows ATR-IR spectra of rich and lean flame soot from these three fuels. The peaks and functional groups are given in Table 3. Few prior studies noticed a stretch from the alkyne≡C−H group (3284 cm^{-1}) for *n*-hexane soot,[21] while it was observed in this work. The peak around 3040 cm^{-1} for *n*-hexane and decane flame soot was assigned to the aromatic C−H stretch,[20,21,40−42] which has been widely detected in hydrocarbon soot and activated carbon. The two peaks at 2918 and 2846 cm^{-1} for toluene and decane flame soot were related to the CH_2 and CH_3 stretch.[20] An absorption band at 1440 cm^{-1} for *n*-hexane soot corresponded to the scissor vibration of unsaturated CH_2.[20,32,41] Three bands in the range of 900−700 cm^{-1} for the three fuels' flame soot were attributed to the substitution modes of aromatic compounds.[20,21,40,41] Several oxygen-related functional groups were also detected in the soot spectra. For example, the main characteristic band for the three fuels' flame soot was at 1590 cm^{-1}, which was assigned to a carbonyl (C═O) group bound to an aromatic ring.[13,20,21,31,40−42] The presence of another

dx.doi.org/10.1021/jp301041w | J. Phys. Chem. A 2012, 116, 4129−4136

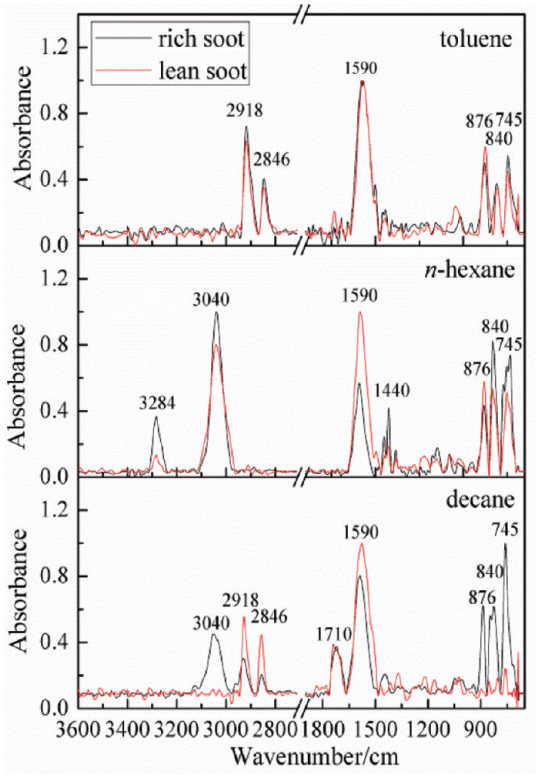

Figure 7. Typical baseline-corrected, normalized ATR-IR spectra for rich and lean toluene, *n*-hexane, and decane soot.

Table 3. Functional Groups Observed for Rich and Lean Toluene, *n*-Hexane, and Decane Soot

peak/cm^{-1}	functional group
3284	alkynes≡C−H stretch
3040	aromatic C−H stretch
2918	alkane CH_2 asymmetric stretch
2846	alkane CH_3 asymmetric stretch
1710	carbonyl C═O
1590	C═O bonded to an aromatic ring
1440	unsaturated C−H(═CH_2) scissor vibration
876	substituted aromatic C−H
840	substituted aromatic C−H
745	substituted aromatic C−H

carbonyl group, assigned to ketone species (1710 cm^{-1}), was observed for decane soot.[13,20,21,40,41]

As seen in Figure 7, compared to the functional groups on the rich toluene flame soot, no significant changes were observed on the lean toluene flame soot. For *n*-hexane and decane soot, the lean flame soot exhibited lower intensities in the peaks of alkynes≡C−H, aromatic C−H, unsaturated CH_2, and highly substituted aromatic compounds, while the carbonyl (C═O) group bound to an aromatic ring showed a larger intensity than that of the rich flame soot. These results demonstrate that combustion conditions have significant effects on composition.

4. DISCUSSION

On the basis of the changes in the parameters L/W, D_f, $\overline{d}_p$, and L_a, it is difficult to directly establish the relationship between the hydrophilicity of soot samples and the physical structure. Therefore, it was necessary to further discuss the influence of chemical structure on the hydrophilicity of soot.

To confirm the influence of VOCs on the hydrophilicity of soot samples, Figure 8 compared the surface tension of the

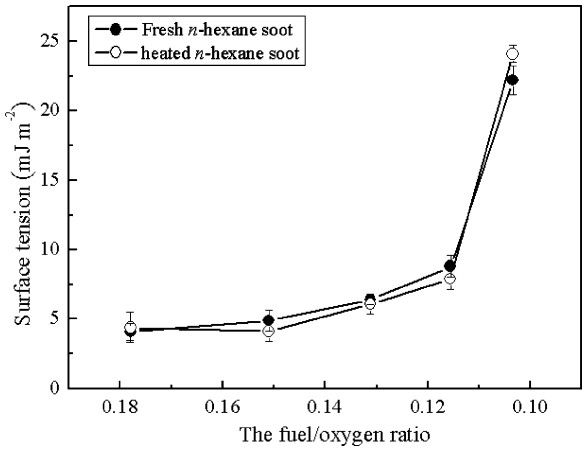

Figure 8. Comparison of surface tension for fresh and 300 °C heated *n*-hexane soot.

fresh and 300 °C heated *n*-hexane soot. Almost no difference was observed between the heated samples and the fresh samples. This confirms that VOCs have little effect on the interaction of soot with water, which may be ascribed to their very low content (35−65 mg/g) on soot. On the other hand, if hydrophilic species are embedded in VOCs, the hydrophilicity of soot will decrease after removing VOCs. However, the observed facts are that hydrophilicity of heated soot remains unchanged suggesting that hydrophilic species should mainly be located in the carbon skeleton of soot rather than in VOCs.

It is well-known that C−H functional groups are hydrophobic while C═O groups are hydrophilic.[16,23,31] Thus, the integrated areas of the absorption peaks in the ATR-IR spectra can be associated to the hydrophilic or hydrophobic character of the organic materials. Table 4 summarizes the relative

Table 4. Changes of the Hydrophobic and Hydrophilic Functional Groups' Intensities

fuels	type of soot	C═O/Ar−H (aromatic C−H)	C═O/R−H (aliphatic C−H)	$T_{C=O}/T_{C-H}$ (total C═O /total C−H)
toluene	rich	1.7	2.6	1.1
	lean	1.8	3.1	1.3
n-hexane	rich	0.3	2.2	0.18
	lean	0.6	7.7	0.56
decane	rich	0.7	5.5	0.65
	lean	6.2	4.5	2.6

intensities of hydrophilic and hydrophobic functional groups. The C═O/Ar−H, C═O/R−H, and $T_{C=O}/T_{C-H}$ (the ratio of peak areas of all hydrophilic groups to peak areas of all hydrophobic groups) ratios for rich and lean toluene flame soot only exhibited a slight increase. This is well in accordance with the small effect of the fuel/oxygen ratio on the changes of contact angle or surface tension for toluene flame soot. Compared to rich *n*-hexane flame soot, lean *n*-hexane flame soot increased by factors of 2 for the ratio C═O/Ar−H and of more than 3 for the ratio C═O/R−H. The lean decane flame soot exhibited a C═O/Ar−H ratio larger by a factor of 8 than

dx.doi.org/10.1021/jp301041w | J. Phys. Chem. A 2012, 116, 4129−4136

that of rich decane flame soot. Additionally, the increase in amplitude in $T_{C=O}/T_{C-H}$ for lean *n*-hexane and decane flame soot was 2 and 3 factors. Considering the convenience of the preparation of *n*-hexane flame soot through the present method, the surface tension values have been plotted versus $T_{C=O}/T_{C-H}$ of *n*-hexane soot obtained in the range of (0.180−0.100) of the fuel/oxygen ratio in Figure 9. It can be seen that

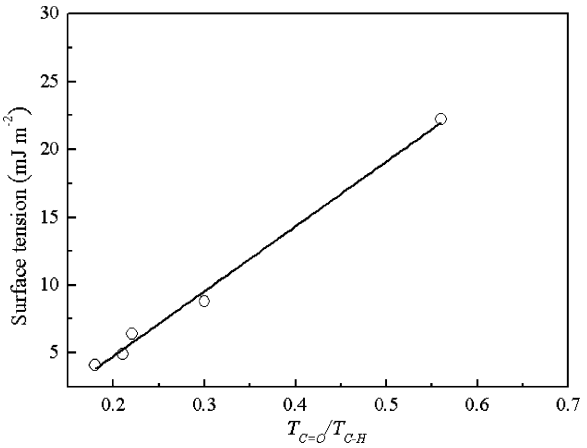

Figure 9. Plot of surface tension versus $T_{C=O}/T_{C-H}$ for *n*-hexane flame soot.

surface tension increases linearly with $T_{C=O}/T_{C-H}$ demonstrating that more oxygen-related species can contribute to stronger hydrophilicity in lean flame soot.

We also investigated the $T_{C=O}/T_{C-H}$ ratio for heated rich and lean *n*-hexane soot, which was 0.25 and 0.66, showing a slight increase that cannot induce significant changes in hydrophilicity. After removal of VOCs, the larger $T_{C=O}/T_{C-H}$ ratio further confirmed that hydrophilic species were located in the carbon skeleton of soot rather than in VOCs, which coincided well with results proposed by Akhter et al.[40] They stated that some oxygen-related functionalities such as carbonyl, ether, and anhydride groups were incorporated in the graphitic structure that formed the skeleton of soot. To identify microscopic regions containing hydrophilic species in the soot skeleton, the parameter $T_{C=O}/T_{C-H}$ was plotted against the parameter $I_{(D1+D2)}/I_G$ for three fuels' flame soot (Figure 10). As shown in Figure 10, the parameter $T_{C=O}/T_{C-H}$

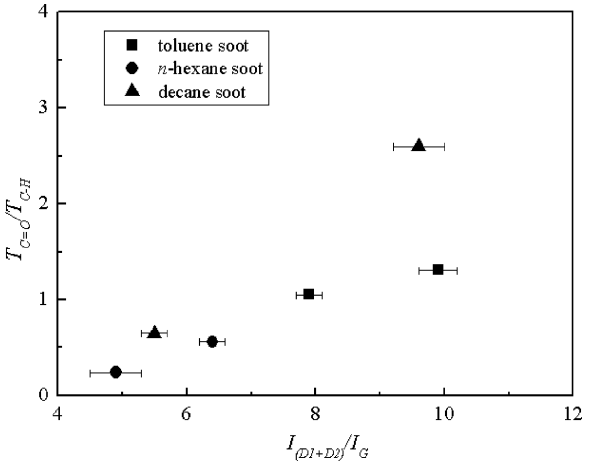

Figure 10. Plot of parameter $T_{C=O}/T_{C-H}$ versus parameter $I_{(D1+D2)}/I_G$.

displayed an increasing trend with an increase in the parameter $I_{(D1+D2)}/I_G$. This means that hydrophilic functional groups (C═O) might be mainly located at graphene layer edges and surface graphene layers. According to the results of Raman spectra, a higher content of disordered carbon at graphene layer edges and surface graphene layers for lean *n*-hexane and decane flame soot can be one of the reasons for their smaller contact angle and larger surface tension. This also suggests that the lower degree of structural order of soot may also result from the incorporation of oxygen-containing groups into the graphene structure, which then contribute to the stronger hydrophilicity of soot. In comparing rich and lean toluene flame soot, although the latter had a lower degree of structural order, it did not show stronger hydrophilicity because of the insignificant increase in amplitude in the C═O/Ar−H, C═O/Ar−H, and $T_{C=O}/T_{C-H}$ ratios. The difference in soot formation mechanism upon pyrolysis of aliphatic and aromatic hydrocarbon fuels may explain the reason why toluene data deviates from the data for *n*-hexane and decane (Figure 2). It is believed that polycyclic aromatic hydrocarbons (PAHs) are the key intermediate compounds in soot formation.[43−46] The formation of the first aromatic ring is perceived to be the rate-limiting step in the reaction sequence to larger aromatics.[43,44] In flame of nonaromatic fuels, the formation of the first aromatic ring starts with the joining of small aliphatics (C_4H_3, C_2H_2, C_3H_3, C_5H_5, et al.).[43,44] Numerical simulations have identified oxidation of small aliphatics as the key point of branching between aromatics growth and aromatics oxidation.[45,46] Thus, oxygen-containing groups might be more favorably formed at low fuel/oxygen ratio for *n*-hexane and decane combustion compared to toluene combustion. On the basis of the above results, it may be concluded that the ratio between hydrophilic and hydrophobic functional groups and the content of disordered carbon at graphene layer edges and surface graphene layers reflect the chemical properties of soot with respect to its hydrophilicity. These results confirm that combustion conditions can affect the hydrophilic properties of soot by altering its functional groups and chemical microstructure.

5. CONCLUSIONS

Soot samples were produced under controlled combustion conditions. Surface tensions for *n*-hexane and decane flame soot exhibited a significant increase with decreasing fuel/oxygen ratio, while that for toluene flame soot almost remained unchanged. These results suggest that combustion conditions play different roles in hydrophilic changes for soot of different origins.

The fuel/oxygen ratio has a little effect on physical structure changes including maximum length (L) to average width of aggregates (W), fractal dimension (D_f), and graphite crystallite size (L_a). However, average particle diameter ($\bar{d}_p$) and content of VOCs decreased with decreasing fuel/oxygen ratio. Because of the low content of VOCs on flame soot, their influence on the hydrophilic changes of soot was negligible. On the basis of the infrared spectral results, it was found that the surface tension of soot samples increases linearly with the ratio of C═O content to C−H content, which greatly depends on combustion conditions. On the basis of Raman and infrared spectra, it is suggested that hydrophilic functional groups were mainly located at the graphene layer edges and surface graphene layers of the carbon skeleton in soot.

AUTHOR INFORMATION

Corresponding Author

*E-mail: ycliu@rcees.ac.cn (Y.L.); honghe@rcees.ac.cn (H.H.).

Notes

The authors declare no competing financial interest.

ACKNOWLEDGMENTS

This research was financially supported by the National Natural Science Foundation of China (20907069, 50921064, and 20937004).

REFERENCES

(1) Chameides, W. L.; Bergin, M. *Science* **2002**, *297*, 2214−2215.
(2) Menon, S.; Hansen, J.; Nazarenko, L.; Luo, Y. *Science* **2002**, *297*, 2250−2253.
(3) Jacobson, M. Z. *Nature* **2001**, *409*, 695−697.
(4) Sydbom, A.; Blomberg, A.; Parnia, S.; Stenfors, N.; Sandström, T.; Dahlén, S. E. *Eur. Respir. J.* **2001**, *17*, 733−746.
(5) Monge, M. E.; D'Anna, B.; Mazri, L.; Giroir-Fendler, A.; Ammann, M.; Donaldson, D. J.; George, C. *Proc. Natl. Acad. Sci. U. S. A.* **2010**, *107* (15), 6605−6609.
(6) Arens, F.; Gutzwiller, L.; Baltensperger, U.; Gaggeler, H. W.; Ammann, M. *Environ. Sci. Technol.* **2001**, *35*, 2191−2199.
(7) Kleffmann, J.; Becker, K. H.; Lackhoff, M.; Wiesen, P. *Phys. Chem. Chem. Phys.* **1999**, *1*, 5443−5450.
(8) Zhang, D.; Zhang, R. *Environ. Sci. Technol.* **2005**, *39*, 5722−5728.
(9) Lelièvre, S.; Bedjanian, Y.; Pouvesle, N.; Delfau, J.; Vovelle, C.; Bras, G. L. *Phys. Chem. Chem. Phys.* **2004**, *6*, 1181−1191.
(10) Stadler, D.; Rossi, M. J. *Phys. Chem. Chem. Phys.* **2000**, *2*, 5420−5429.
(11) Munozy, M. S. S.; Rossi, M. J. *Phys. Chem. Chem. Phys.* **2002**, *4*, 5110−5118.
(12) Lelièvre, S.; Bedjanian., Y.; Laverdet, G.; Bras, G. L. *J. Phys. Chem. A* **2004**, *108*, 10807−10817.
(13) Daly, H. M.; Horn, A. B. *Phys. Chem. Chem. Phys.* **2009**, *11*, 1069−1076.
(14) Mccabe, J.; Abbatt, J. P. D. *J. Phys. Chem. C* **2009**, *113*, 2120−2127.
(15) Dippel, B.; Jander, H.; Heintzenberg, J. *Phys. Chem. Chem. Phys.* **1999**, *1*, 4707−4712.
(16) Popovicheva, O. B.; Persiantseva, N. M. *J. Phys. Chem. A* **2003**, *107*, 10046−10054.
(17) Knauer, M.; Schuster, M. E.; Su, D.; Schlögl, R.; Niessner, R.; Ivleva, N. P. *J. Phys. Chem. A* **2009**, *113*, 13871−13880.
(18) Müller, J. O.; Su, D. S.; Wild, U.; Schlögl, R. *Phys. Chem. Chem. Phys.* **2007**, *9*, 4018−4025.
(19) Sadezky, A.; Muckenhuber, H.; Grothe, H.; Niessner, R.; Pöschl, U. *Carbon* **2005**, *43*, 1731−1742.
(20) Cain, J. P.; Gassman, P. L.; Wang, H.; Laskin, A. *Phys. Chem. Chem. Phys.* **2010**, *12*, 5206−5218.
(21) Kirchner, U.; Scheer, V.; Vogt, R. *J. Phys. Chem. A* **2000**, *104*, 8908−8915.
(22) Ivleva, N.; Messerer, A.; Yang, X.; Niessner, R.; Pöschl, U. *Environ. Sci. Technol.* **2007**, *41*, 3702−3707.
(23) Liu, Y.; Liu, C.; Ma, J.; Ma, Q.; He, H. *Phys. Chem. Chem. Phys.* **2010**, *12*, 10896−10903.
(24) Persiantseva, N. M.; Popovicheva, O. B.; Shonija, N. K. *J. Environ. Monit.* **2004**, *6*, 939−945.
(25) Popovitcheva, O. B.; Persiantseva, N. M.; Trukhin, M. E.; Rulev, G. B.; Shonija, N. K.; Buriko, Y. Y.; Starik, A. M.; Demirdjian, B.; Ferry, D.; Suzanne, J. *Phys. Chem. Chem. Phys.* **2000**, *2*, 4421−4426.
(26) Alcala-Jornod, C.; Rossi, M. J. *J. Phys. Chem. A* **2004**, *108*, 10667−10680.
(27) Alcala-Jornod, C.; Bergh, H. V. D.; Rossi, M. J. *Phys. Chem. Chem. Phys.* **2000**, *2*, 5584−5593.
(28) Jammoul, A.; Gligorovski, S.; George, C.; D'Anna, B. *J. Phys. Chem. A* **2008**, *112*, 1268−1276.
(29) Dubowski, Y.; Vieceli, J.; Tobias, D. J.; Gomez, A.; Lin, A.; Nizkorodov, S. A.; McIntire, T. M.; Finlayson-Pitts, B. J. *J. Phys. Chem. A* **2004**, *108*, 10473−10485.
(30) Sumner, A. L.; Menke, E. J.; Dubowski, Y.; Newberg, J. T.; Penner, R. M.; Hemminger, J. C.; Wingen, L. M.; Brauers, T.; Finlayson-Pitts, B. J. *Phys. Chem. Chem. Phys.* **2004**, *6*, 604−613.
(31) Nieto-Gligorovski, L.; Net, S.; Gligorovski, S.; Zetzsch, C.; Jammoul, A.; D'Anna, B.; George, C. *Phys. Chem. Chem. Phys.* **2008**, *10*, 2964−2971.
(32) Zelenay, V.; Monge, M. E.; D'Anna, B.; George, C.; Styler, S. A.; Huthwelker, T.; Ammann, M. *J. Geophys. Res.* **2011**, *116*, D11301.
(33) Kwok, D. Y.; Neumann, A. W. *Adv. Colloid Interface Sci.* **1999**, *81*, 167−249.
(34) Slowik, J. G.; Cross, E. S.; Han, J. H.; Kolucki, J.; Davidovits, P.; Williams, L. R.; Onasch, T. B.; Jayne, J. T.; Kolb, C. E.; Worsnop, D. R. *Aerosol Sci. Technol.* **2007**, *41*, 734−750.
(35) Slowik, J. G.; Stainken, K.; Davidovits, P.; Williams, L. R.; Jayne, J. T.; Kolb, C. E.; Worsnop, D. R.; Rudich, Y.; DeCarlo, P. F.; Jimenez, J. L. *Aerosol Sci. Technol.* **2004**, *38*, 1206−1222.
(36) Escribano, R.; Sloan, J. J.; Siddique, N.; Sze, N.; Dudev, T. *Vib. Spectrosc.* **2001**, *26*, 179−186.
(37) Knight, D. S.; White, W. B. *J. Mater. Res.* **1989**, *4* (2), 385−393.
(38) Schwan, J.; Ulrich, S.; Batori, V.; Ehrhardt, H. *J. Appl. Phys.* **1996**, *80* (1), 440−447.
(39) Shroder, R. E.; Nemanich, R. J. *Phys. Rev.* **1990**, *41*, 3738−3745.
(40) Akhter, M. S.; Chughtai, A. R.; Smith, D. M. *Appl. Spectrosc.* **1985**, *39*, 143−153.
(41) Smith, D. M.; Chughtai, A. R. *Colloids Surf.* **1995**, *105*, 47−77.
(42) Smith, D. M.; Akhter, M. S.; Jassim, J. A.; Sergides, C. A.; Welch, W. F.; Chughtai, A. R. *Aerosol Sci. Technol.* **1989**, *10*, 311−325.
(43) Frenklach, M. *Phys. Chem. Chem. Phys.* **2002**, *4*, 2028−2037.
(44) Mansurov, Z. A. *Combust., Explos. Shock Waves* **2005**, *41* (6), 727−744.
(45) Frenklach, M.; Warnatz, J. *Combust. Sci. Technol.* **1987**, *51*, 265−283.
(46) Frenklach, M.; Clary, D. W.; Yuan, T. *Combust. Sci. Technol.* **1986**, *50*, 79−115.